Biosensors and Bioelectronics 145 (2019) 111717

Contents lists available at ScienceDirect

Biosensors and Bioelectronics

journal homepage: www.elsevier.com/locate/bios

Wavelength-scanning surface plasmon resonance microscopy: A novel tool for real time sensing of cell-substrate interactions

Youjun Zeng[1], Jie Zhou[1], Xueliang Wang, Zhiwen Cai, Yonghong Shao[*]

College of Physics and Optoelectronics Engineering, Key Laboratory of Optoelectronic Devices and Systems of Ministry of Education and Guangdong Province, Shenzhen Key Laboratory of Sensor Technology, Shenzhen University, Shenzhen, 518060, China

ARTICLE INFO

Keywords:
Surface plasmon resonance microscope (SPRM)
Wavelength scanning
Cell-substrate interaction
Electroporation

ABSTRACT

This paper, for the first time, presents a wavelength-scanning surface plasmon resonance microscope (WS-SPRM) as a label-free biosensor capable of measuring cell-substrate interaction. The approach utilized a liquid crystal tunable filter (LCTF) as a fast and flexible wavelength-scanning device that can implement a wavelength-scanning and SPR imaging cycle within 1 s. The system was verified by monitoring the dynamics of cellular processes including cell detachment and electroporation of individual cells. It was found that the WS-SPRM presented better performance than the intensity-based SPRM (I-SPRM) in the imaging of cell adhesion. The results also indicated that the WS-SPRM exhibited a larger dynamic range in monitoring cell electroporation than that of I-SPRM. In summary, the developed WS-SPRM in this study provides a promising technique for real-time monitoring of cell-substrate interaction.

1. Introduction

Cell adhesion is an essential process in cell growth, cell migration, cell communication and regulation. It plays an essential role in many physiological phenomena such as the development and maintenance of tissues, wound healing, tumor metastasis, etc. (Khalili and Ahmad, 2015; Lidstone et al., 2011; Ungai-Salanki et al., 2019). The cell-substrate interactions affect the adhesion behavior of cells significantly and needs to be investigated for exploring the mechanism of cell adhesion. A continuously increasing demand has emerged in developing non-invasive and label-free techniques to realize real-time observation of cell-substrate interactions. To date, the potential of cell-based biosensors, such as electric impedance spectroscopy (EIS) sensors (Jie et al., 2013; Susloparova et al., 2015), quartz crystal microbalance (QCM) sensors (Chen et al., 2012; Reyes et al., 2013) and optical sensors based on extraordinary optical transmission (EOT) (Tu et al., 2017) have already been demonstrated for monitoring cell–substrate interactions. SPR-based biosensors represent as another promising tool to study the interactions between cells and the substrate owing to its advantages of label-free, non-invasiveness and high sensitivity (Abadian et al., 2014; Yanase et al., 2014; Zeidan et al., 2015).

SPR sensing technology has been steadily gaining popularity for exploring the molecular interactions by detecting the refractive index changes induced by the binding and dissociation of molecules on a gold-coated chip in the last three decades (Hegnerová and Homola, 2010; Horii et al., 2011; Wang et al., 2016). It has been extensively applied in various fields such as biochemical analysis, drug research and development (Olaru et al., 2015; Retra and Irth, 2011), disease diagnosis (Altintas and Fakanya) and environmental monitoring (Fen and Yunus, 2013). Moreover, with the growing availability and new technological advances, SPR sensors have increasingly been used to investigate other biological systems beyond traditional molecular binding (Abadian et al., 2014), such as membranes (Figueira et al., 2017; Jennifer A. Maynard, 2009), bacterial cells(Baccar et al., 2010; Wang et al., 2013) and mammalian cells (Stojanović et al., 2014; Yanase et al. 2013, 2016).

SPR imaging (SPRi), which combines the SPR sensing technology with an imaging equipment, enables high-throughput biosensing in two-dimensional microarrays and parallel monitoring of multiple biomolecular interactions on a chip surface (Zeng et al., 2017). Moreover, the spatial resolution of SPRi could be greatly increased by introducing an objective into the imaging system (Shinohara et al., 2013; Yanase et al., 2012) or by replacing the prism with a high numerical aperture (NA) objective (Wang et al. 2011, 2012), which is also refereed as the SPR microscope (SPRM). The SPRM has widely been applied for single cell imaging (Yanase et al., 2010) and studying cellular activities, including the cell interactions with surfaces (Wang et al., 2012) and cell physiologic changes due to extracellular stimulations (Wang et al.,

* Corresponding author.
E-mail address: shaoyh@szu.edu.cn (Y. Shao).
[1] These authors contributed equal to the article.

https://doi.org/10.1016/j.bios.2019.111717
Received 18 July 2019; Received in revised form 5 September 2019; Accepted 18 September 2019
Available online 20 September 2019
0956-5663/

2011).

To date, four SPR sensing techniques, involving intensity, wavelength, angular, and phase interrogations, have been widely reported. The intensity-based SPRM (I-SPRM) is typically adopted in the analysis of living cells because of its simple optical setup, convenient operation and high imaging speed (Horii et al., 2011; Peterson et al., 2009; Shinohara et al., 2013; Wang et al., 2012; Wei et al., 2012; Yanase et al., 2010). However, the I-SPRM suffers from limited dynamic range. Since the adhesion of cells varies greatly in different areas, the limited dynamic range of the I-SPRM may fail to reflect the real cell–substrate interactions. The angular-interrogated SPR has also been applied in the detection of cell activity (Chabot et al., 2009; Kosaihira and Ona, 2008; Maltais et al., 2012; Ziblat et al., 2006). Compared with the I-SPRM, the angular-interrogated SPR has a wider dynamic range (J Bianca et al., 2008). However, it was rarely exploited in SPR imaging due to its inherent defects. One is that the homochromatic laser typically used as a light source might induce speckles. The other is that, in the prism structure, varying degrees of distortion would occur during the imaging of the sensor surface when scanning at different incident angles, which might affect the quality of imaging results.

Wavelength-scanning SRP (WS-SPR) can achieve a high sensitivity and wide dynamic range that are similar to that in the angular-interrogated SPR. Moreover, it can flexibly select the best excitation wavelength for different areas on the chip, which is beneficial for high-throughput detection in SPR imaging. However, it has never been applied in the development of SPR microscope (SPRM) to the analysis of living cells so far, which might be attributed to its relatively low time resolution. In our previous work, a fast WS-SPRi biosensing system using liquid crystal tunable filter (LCTF) was developed for real-time and high-throughput detection of biomolecular interactions (Chen et al., 2016; Zeng et al., 2016). With the use of LCTF and an adaptive spectral-dip tracking scheme, the system is capable of completing an SPR dip measurement within 700 ms (Zeng et al., 2016). The time resolution of the wavelength-interrogated SRP was significantly improved compared to those using a monochromator as the wavelength scanning device. Thus, by utilizing the developed technique, the limitation of the WS-SPRM was resolved, and the WS-SPRM can exhibit its great potential for cell research.

In this paper, a novel WS-SPRM was developed for the first time for monitoring cell-substrate interactions. The approach utilized a LCTF as a fast and flexible wavelength-scanning device to decrease the measurement time for one wavelength-scanning and SPR imaging cycle. We have demonstrated that the new technique could indeed be applied to cell imaging and studying the cell adhesion under extracellular chemical and electrical stimulus.

2. Methods

2.1. The experimental setup

The schematic of the WS-SPRM setup is shown in Fig. 1. The system is consisted of two optical paths: the SPRM path under the cell and the white-light microscopic path over the cell.

In the SPRM path, a halogen lamp is used as the SPR excitation light source. The broad-spectrum light emitted by the halogen lamp is coupled into a multi-mode optical fiber (MF) through a group of lenses. The fiber light passes through the collimating lens group (L1, L2) and diaphragm aperture (DA), and reaches to the liquid crystal tunable filter (LCTF) to acquire a narrow-band light with a specified central wavelength. The parallel narrow-band light eventually excites the surface plasma wave (SPW) on the surface of Au-coated sensing chip coupled by the prism. The prism is an equilateral triangle made of SF11 glass with a refractive index of 1.71. The sensing chip is fabricated by magnetron sputtering which is at first sputtered with a 1 ~ 2 nm Cr adhesive layer and a 48 nm gold sensing layer successively on the SF11 glass substrate with a size of 18 mm × 18 mm. The sensing chip is

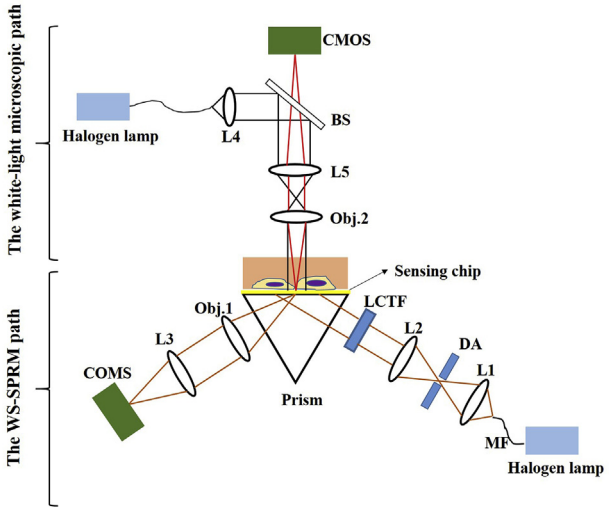

Fig. 1. The schematic of the WS-SPRM setup. Cells are cultured on the SPR sensing chip. The system is consisted of two optical paths: the SPRM path under the cell and the white-light microscopic path over the cell. L1, L2 and L4: Lens; L3 and L5: Tube lens; Obj.1-2: Objects lens; DA: Diaphragm aperture; MF: Multimode optical fiber; BS: Beam splitting.

attached to the prism using refractive index matching oil. The reflected light of the sensing module passes through an objective lens (Obj.1, Nikon, N10 × -PF) and a tube lens (L3, focal length: 150 mm, Thorlab, LA1433A) and is finally recorded by a CMOS (DMK33GP1300) device.

In the SPRM path, the CMOS device is used to image the sensing surface as the LCTF switches the incidence wavelength each time. The gray values of each pixel on the sensing surface at different wavelengths are recorded. During a scanning process, the LCTF constantly switches the wavelength, and the CMOS device continuously images the sensing surface at the same time. When a scanning cycle is completed, the SPR spectral curve of each pixel can be constructed through a series of images. Then the resonance wavelength (RW) of each pixel is obtained by fitting the spectral curves. Consequently, the RW imaging of the sensing surface can be realized. In the experiments, the wavelength scanning range is from 620 nm to 680 nm with a scanning step of 3 nm. The duration for completing a wavelength-scanning and SPR imaging cycle is about 1 s.

The white-light microscope is located above the sensor chip. The white light emitted by the halogen lamp enters a DC voltage-regulated optical fiber source (Daheng optics, CCI-060101) through a coupling lens. The light emitted from the optical fiber is collimated by a lens (L4), a beam splitting (BS, Thorlab, BSW25), in which half of incidence light directly passes through the BS. Meanwhile, the other half of light, as the illumination light, passes through an objective lens (Obj.2, Nikon, N10 × -PF) and a tube lens (L5, focal length: 100 mm, Thorlab, LA1509A) and then irradiates at the surface of the sensing chip. The sensing chip is located at the object plane of the Obj.2. The light illuminates on the sensing surface and is scattered and reflected by the sample. The scattered light and the reflected light pass through the Obj.2 and L5 in turn and are finally recorded by the CMOS device to realize the sample imaging on the chip surface. In the experiments, the white light microscopy path is controlled by two one-dimensional displacement tables that can control the imaging area and a high-precision elevatorthat is used to adjust the distance between the microscopy path and the sensor chip.

2.2. Data processing and algorithms

The acquired SPR spectral data needs to be fitted to get the RW for each pixel in a series of images captured by the CMOS device. Typically, the SPR spectral curve is fitted by a high-order nonlinear function, and

higher fitting order can result in a smoother fitting curve and higher calculation precision. For instance, the spectral curve with a spectral width of 100 nm should be fitted by a 10-order nonlinear function. However, with the increasing of the fitting order, the influence of random noise on the curve shape is also increased, which may induce miscalculation of the RW. In order to acquire high-precision fitting spectrum as well as reduce the influence of random noise on the curve shape, we proposed a nonlinear fitting method with a fixed curve model and verified its effectiveness both in stimulation and in experiments.

In the simulation, we first stimulated an ideal SPR spectral curve by Fresnel equations. Then the curve was fitted with 7-order polynomial fitting. The polynomial coefficients were chosen to be the best fitting parameters and used to describe the curve model. Then we added random white noise to the ideal SPR curve to simulate the real SPR spectral data. The simulated SPR data was calculated iteratively by the Levenberg-Marquardt algorithm using the best fitting parameters to obtain the fitting curve (MORE, 1978). When the weighted root mean square error (WRMSE) of the fitting curve and the curve model reached the minimum, the calculated SPR spectral curve was chosen as the best fitting curve. The shape of the best fitting curve coincides with that of the model curve. Levenberg-Marquardt algorithm was employed in our study since it combined the advantages of Gauss-Newton algorithm and gradient descent algorithm and can provide numerical solution of nonlinear minimization (local minimization). We employed the direct high-order fitting method and the proposed fitting method to fit two hundreds simulated SPR spectral data and obtained the RW through the fitting results. As shown in Fig. 2(a), the nonlinear fitting method with a fixed curve model has lower noise than that of the direct high-order fitting methods.

In the experiment, the curve model was obtained by averaging spectral curves of pixels in cell areas over a period of time when cell condition was stable. Then the direct high-order fitting method and the nonlinear fitting with a fixed curve model were applied to fit the acquired SPR spectral data for each pixel. The real-time RW changes of cell region obtained by these two methods are shown in Fig. 2(b). As shown in the figure, the nonlinear fitting with a fixed curve model method has much smaller noise than that of the direct high-order fitting method. Typically, the spectral curve with a spectral width of 60 nm should be fitted by a 7-order nonlinear function. However, in our experiment, the fitting order was chosen to be 5 since the error of RW obtained by the 5-order fitting method is less than the spectral resolution of LCTF (0.01 nm) and the 5-order fitting method is relatively insensitive to the random noise. The above results validate that the nonlinear fitting method with a fixed curve model performs better than the direct high-order fitting method.

2.3. Cell culturing

The HeLa cell line was derived from ATCC cell bank. The cells were cultured in DEME medium (Hyclone) containing 10% fetal bovine serum (Gibco) and 1% penicillin and streptomycin at 37 °C in a humidified incubator with 5% CO_2. The cells in flasks were passaged every 2-3 days. To seed HeLa cells on the gold chip, 400 μl growth medium with 12,000 cells were added to a PDMS culturing well that was adhered on the chip. The chip was then put into a culture dish and placed in the cell incubator. After the incubation for 24 h, the chip was taken out from the culture dish and attached to the prism using the refractive index matching oil. The experiments were carried out at room temperature.

2.4. Acute cell responses and electroporation

To induce acute cellular responses, 1% Triton X-100 or 0.25% trypsin (both prepared in DMEM) was added into the wells before SPR measurements. For electroporation, 1 KHz a.c. modulation with a Vpp of 20 V was applied on the electrode using a signal generator for a duration time of 10 s, 20 s and 40 s.

3. Results and discussions

3.1. System optimization

Since the WS-SPRM exploited the Kretschmann prism as the coupling device, aberration would occur when imaging the sensing surface. Laplatine et al. discussed the causes of aberration and optimization methods for decreasing the imaging aberration in a prism-coupled SPRM (Laplatine et al., 2014). They concluded that in the prism-coupled SPRM, when the light was incident perpendicularly to the oblique edge of the prism, the sensing surface can be imaged without aberration under ideal conditions.

Generally, the refractive index of cells ranges from 1.333 RIU to 1.370 RIU, and the scanning wavelength normally ranges from 600 nm to 700 nm to excite the SPR phenomenon in our SPR technology. Therefore, a specific prism should be selected to keep the RW of cells on the chip surface being within the scanning wavelength range when the incident light is perpendicular to the oblique edge of the prism. In the experiments, the equilateral prism with higher refractive index made of

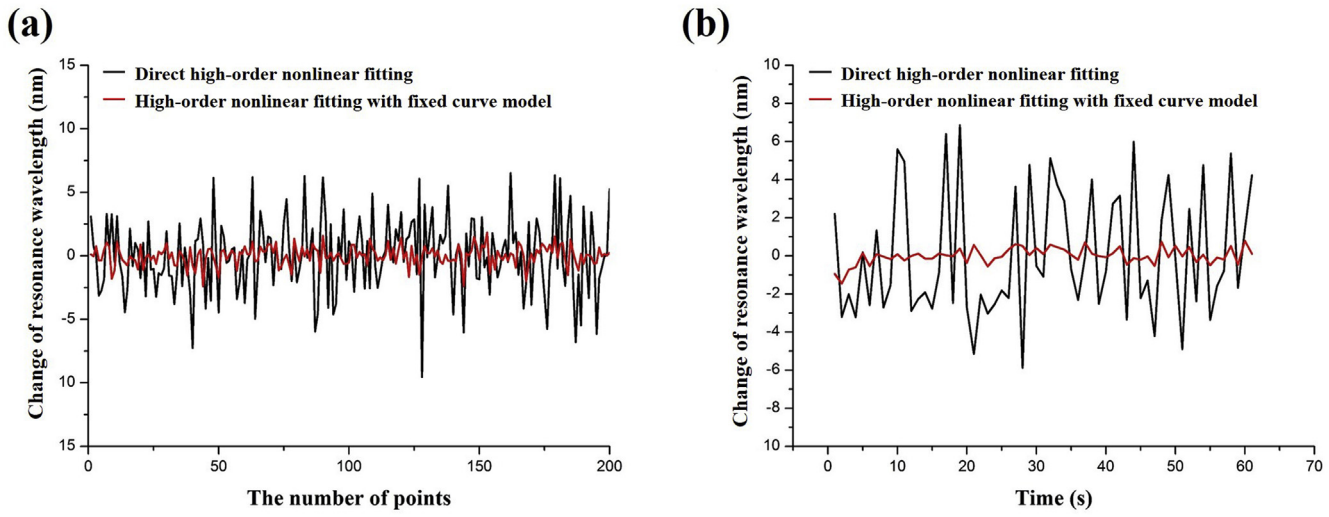

Fig. 2. (a) Simulation results of the RW calculated by the direct high-order fitting method and the proposed fitting method. (b) Experimental results of the RW calculated by the direct high-order fitting method and the proposed fitting method.

SF11 (refractive index: 1.71 RIU) glass was chosen as the coupling device to decrease the SPR excitation angle. Under the stimulation, the incident light was incident perpendicularly to the oblique edge of the prism, and the refractive index of samples was chosen to be within the refractive index range of cells. For SF11, the RW for these samples was exactly within wavelength scanning range (600 nm–700 nm).

The objective lens in the microscope determines the magnification rate, imaging resolution, etc.. Therefore, an objective lens should be carefully considered for the prism-based WS-SPRM. Firstly, the reflected light of the sensing surface needs to pass through the prism and reaches to the objective lens. Thus, the working distance of objective lens should to be larger than 10 mm. In addition, the optical path of the reflected light from the sensing surface to the objective lens is not identical for different detection sites on the sensing surface. Consequently, an objective lens with large field depth should be exploited in order to clearly image larger area on the sensing surface. Lastly, the numerical aperture of the objective lens partially determines the spatial resolution of the SPRM. In conclusion, based on the above-mentioned issues, we selected the N10X-PF (Nikon) as the objective lens with a magnification of 10×, NA of 0.3, working distance of 16 mm and field depth of 8.5 μm.

3.2. The comparison of the WS-SPRM and I-SPRM for NaCl detection and single cell imaging

To compare the dynamic range of WS-SPRM and I-SPRM, various concentrations of NaCl were detected in two modes. At first, a 3×3 array of ROIs of the same size with even distribution on the sensing surface was selected. NaCl solutions (prepared using deionized Milli-Q water) at concentrations ranging from 0 to 25% in increments of 5% by volume (corresponding to a refractive index ranging from 1.333 to 1.37925 RIU) were then injected. In the experiments, the incident wavelength (600 nm–700 nm) was continuously scanned to acquire the SPR spectral curve for each ROI. Then, the real-time RW was obtained by analyzing the spectral curve. The light intensity of each ROI was also acquired by the intensity of a fixed wavelength on the spectral curve. The wavelength for I-SPRM was selected in the linear range of the SPR spectral curve obtained in the first scanning of wavelength.

The relationship between the refractive index and the intensity shift and RW shift is shown in Fig. 3(a-b). Each point represents the mean ± SD of nine ROIs. It is seen from this figure that the intensity has linear relationship with the refractive index in the refractive index range of 1.333 RIU-1.3515 RIU ($r^2 = 0.992$) and the RW has linear relationship with the refractive index in the refractive index range of 1.333 RIU-1.37925 RIU ($r^2 = 0.998$). Thus the dynamic range of I-SPRM and WS-SPRM system are 1.85×10^{-2} RIU and 4.625×10^{-2} RIU. Since the adhesion of cells varies greatly in different areas, the WS-SPRM would have unique advantages for cell imaging due to wider dynamic range. Furthermore, we compared the capability of the SPRM based on intensity interrogation and wavelength interrogation for single cell imaging.

Fig. 3(c) presents the intensity image of a single cell acquired by the I-SPRM. The incident wavelength was obtained by subtracting 20 nm from the average RW of pixels in the cell region, at which the intensity varies linearly with the change of the refractive index. For the cell in the image, the incident wavelength was calculated to be 621 nm. As shown in the figure, several cell areas cannot be observed in the image acquired by the I-SPRM. The dynamic range of I-SPRM wad about 1.85×10^{-2} RIU. While the refractive index range of cells on the chip surface was about 3.5×10^{-2} RIU, which was calculated by the difference of RW on the cell region (Fig. 3(d)). Thus the SPR response at some sites exceeded the dynamic range of the I-SPRM. Therefore, the I-SPRM results can hardly ensure that the intensity of all pixels can accurately reflect their true SPR conditions when the refractive index of different sites on the sensor surface varies greatly.

Fig. 3(d) showed the RW image of a single cell acquired by the WS-SPRM. As shown in the figure, the cell has a clear profile and better morphologic integrality compared with that in the I-SPRM image. At this interrogation, we could obtain the RW for each pixel, which reflects the real SPR condition of each detection site and induces better detection consistency. Moreover, the variation of cell adhesion could be accurately reflected by the difference in RW. From the above results, it is demonstrated that the WS-SPRM can achieve better performance than the I-SPRM for single cell imaging.

3.3. Cell detachment monitoring under the stimulus of trypsin and Triton X-100

Trypsin and Triton X-100 could both induce acute cell detachment by digesting extracellular matrix proteins and dissolving the lipid bilayer of plasma membrane, respectively. Therefore, the two reagents were used to verify the capacity of the WS-SPRM for measuring the cell-substrate interaction. Fig. 4(a) shows the RW images of a single cell undergoing trypsinization. It could be clearly observed that the RW of cell region gradually reduced when the trypsin took effect on cells. In the meantime, the cell adherent area became smaller due to the shrinkage of the cell. After 80 s of chemical treatment, the RW of most cell regions decreased to that of the background, and the cell became a small dot eventually. It could also be confirmed by the time-dependent RW changes of different regions at cell area shown in Fig. 4 (b). The region of interested 1(ROI 1) is located at the cell center area, while ROI 2 is located at the cell edge area (Fig. 4 (a)). The RW of ROI 2 decreased earlier than that of ROI 1 since the cell edge area was the first to detach from the substrate and shrink after trypsin took effects on the extracellular matrix protein. At the end of trypsinization, the cell almost completely detached from the substrate, and the RW of ROI 1 and ROI 2 reached a plateaus same as that of the background shown in ROI 3.

The RW images of cells undergoing the treatment of Triton X-100 are shown in Fig. S1(a). In the images, the RW of cell region decreased rapidly with the addition of Triton X-100. Moreover, the RW of some cell areas decreased to that of the background at 10 s, illustrating the complete detachment of cells by the dissolution of Triton X-100. The time-dependent RW changes of different regions at cell area displayed in Fig. S1(b) indicated that Triton X-100 dissolved cell membrane uniformly. Notably, visible cell residues or incomplete cell detachment can still be observed after extended trypsinization and Triton X-100 exposure, and these residues could be removed thoroughly with washing steps. The above results of the WS-SPRM for monitoring the real-time cell detachment under the treatment of trypsin and Triton X-100 have proved that the WS-SPRM could be applied for the sensing of cell-substrate interaction.

3.4. Electroporation monitoring

We have also exploited the WS-SPRM to study electroporation, a phenomenon that the membrane permeability of cells can be instantaneously enhanced through the effect of a high intensity electric field so as to absorb extracellular molecules in the surrounding medium. We recorded the RW images and optical images of electroporation processes with different durations. Fig. 5 shows a sequence of optical images (Fig. 5(a)) and RW images (Fig. 5(b)) of an electroporation process with an electrical stimulation duration of 10 s (started at 10s, ended at 20s). The optical images present negligible changes during the electroporation process. As a contrast, the RW images reveal significant changes during the process. The RW of cell regions decreased in varying degrees as the electrical stimulation lasted for different time, indicating local detachment of the cell membrane from the surface. As the electrical stimulation progressed, several prominent perforated areas appeared on cells, and the RWs of these perforated regions decreased to that of the background because the electroporation created openings in the cell membranes. When the electrical stimulation was stopped, the RWs of cell region gradually recovered to the pre-

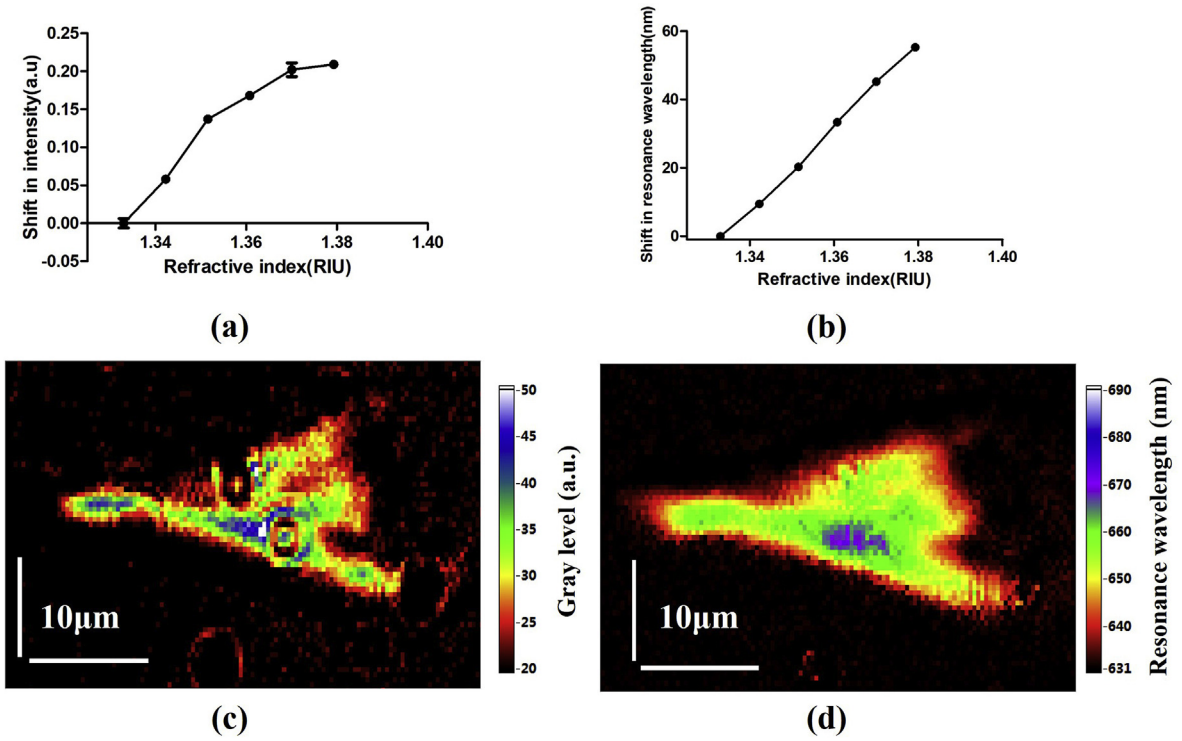

Fig. 3. (a) The relationship between the intensity shift and the increasing refractive index. (b) The relationship between the resonance dip shift with the increasing refractive index. Each point represents the mean ± SD of nine ROIs. (c) The intensity image of a single cell acquired by the I-SPRM. (d) The RW image of a single cell acquired by the WS-SPRM.

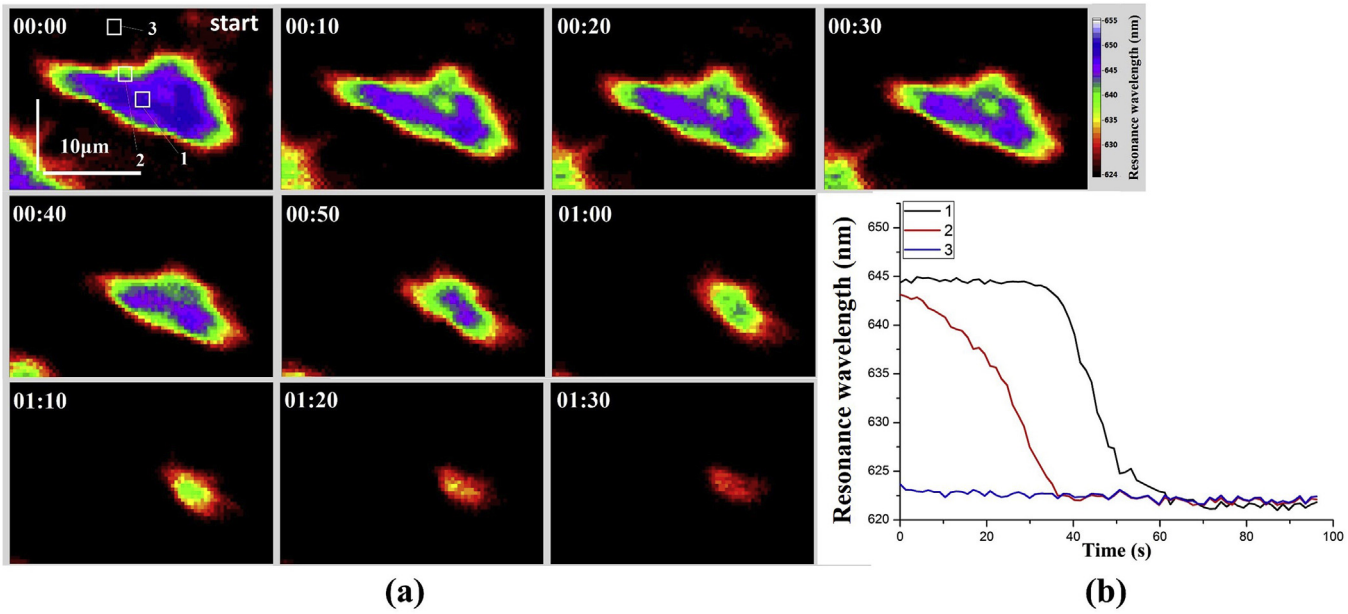

Fig. 4. Cell detachment monitoring under the stimulus of trypsin. (a) The RW images of a single cell undergoing trypsinization. The time format in the images is set to mm: ss. The same below. (b) The time-dependent RW changes of ROIs.

stimulus level.

The time-dependent RW changes of different regions (Fig. 5(c)) at two cells (ROI 1, ROI 2, ROI 3 and ROI 4) and background area (ROI 5) are shown in Fig. 5(d). The electrical stimulation did not affect the SPR conditions of the gold film and culture medium since the RW of ROI 5 barely changed during the electrical stimulation process. Thus, the RW changes of cell region were solely caused by the cellular physiological changes. The RWs of ROI 1-4 decreased rapidly during the electrical stimulation process and then gradually increased when the electrical stimulation was stopped. The RWs reached to a plateau over 50 s. It was apparently observed that the RW change was not uniform across the entire cell as the SPR responses of ROI 1 and ROI 3 were much larger than that of ROI 2 and ROI 4. The reason is that only partial cell area underwent electroporation, thus resulting in the different RW changes in different sites. It is worth noting that the RW did not fully recovered to pre-stimulus level due to the damage of electrical stimulation to cells, and full recovery of cells can usually take hours (Wang et al., 2011).

Figure. S2-3 shows a sequence of RW images of the electroporation

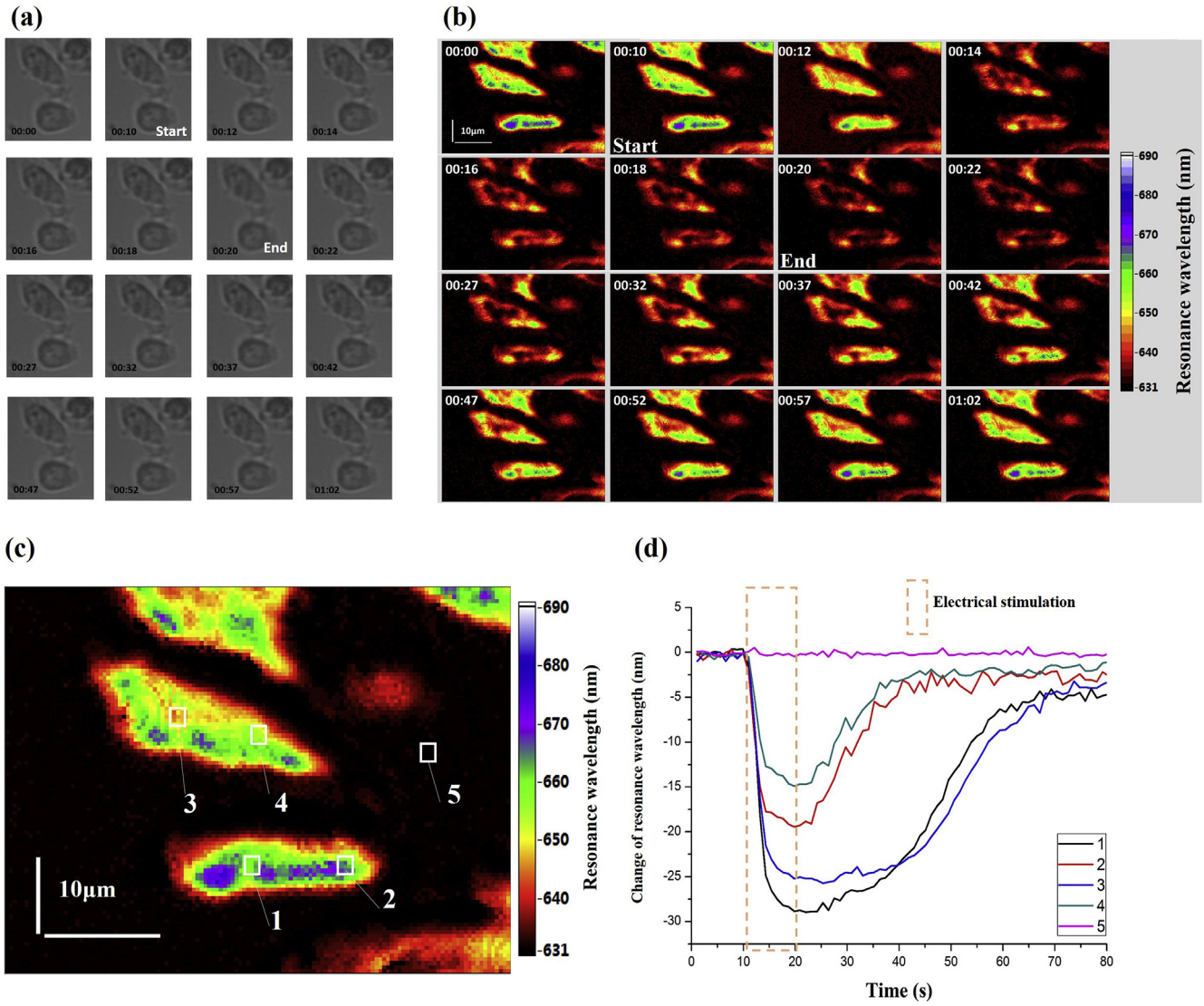

Fig. 5. The optical images (a) and RW images (b) of an electroporation process when the duration of electrical stimulation was 10 s. (c) The RW image of cells before the electrical stimulation, indicating the location of ROIs. (d) The time-dependent RW changes of ROIs.

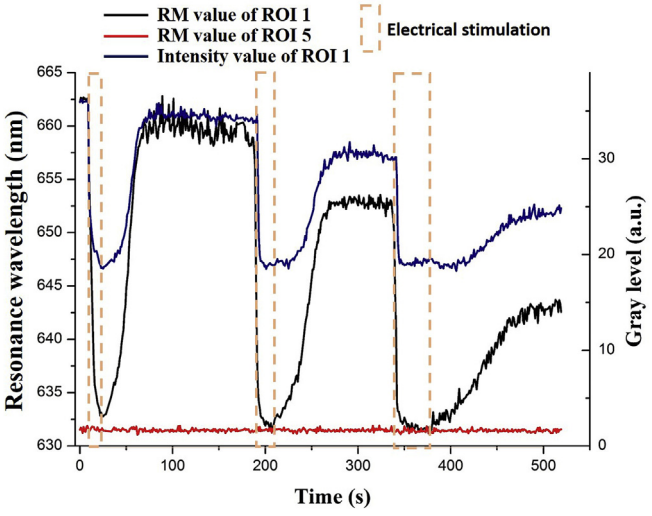

Fig. 6. The time-dependent intensity and RW value of ROI 1 and RW value of ROI 5 during the whole electroporation processes.

process when the duration was 20 s (started at 10s, ended at 30s) and 40 s (started at 10s, ended at 50s). Similarly, the RWs of cell regions decreased rapidly in the first 10 s of the electrical stimulation and started to increase when the electrical stimulation was stopped. Fig. 6 presents the time-dependent RW value of ROI 1 and ROI 5 during the whole electroporation processes, beginning from the 10s of electrical stimulation to the 40s of electrical stimulation. It can be seen that the RW of ROI 1 decreased to the background level at the end of each electrical stimulation. With the extension of stimulation duration, the longer recovery time was required, and the degree of cell recovery became lower. This result is because that the electrical stimulation with longer duration time causes more severe damage to cell viability.

Fig. 6 also displayed the time-dependent intensity value of ROI 1 during the whole electroporation processes. When the duration of electrical stimulation was 10 s, the changing trend of the intensity was consistent with that of the RW, indicating that the intensity could also reflect the electroporation of cells. However, when the duration of electrical stimulation was 20 s and 40 s, the intensity value reduced to a certain degree and remained unchanged until after the electrical stimulation was stopped for several seconds. The results suggested that the SPR response of the cell electroporation region was beyond the dynamic range of the I-SPRM. On the contrary, the RW value continued

to decrease slightly before the electrical stimulation was stopped and then increased immediately when the electrical stimulation was stopped, indicating that the WS-SPRM has larger dynamic range and could monitor intense cell activities in a more accurate manner.

3.5. Discussions

The spatial resolution of the developed WS-SPRM is calculated as 3.96 μm (X axis) and 4.43 μm (Y axis) using the gold nanoparticles, and the field of view the system is 230.4 μm × 297.6 μm. The spatial resolution of our system is limited by several main factors. Firstly, the propagation distance of evanescent wave in metal determines the spatial resolution of the system. Using an incident light with shorter wavelength can reduce the distance of evanescent wave propagation distance and improve the spatial resolution. Under these circumstances, the spatial resolution further depends on the numerical aperture of the objective. An objective lens with high numerical aperture would help increase the spatial resolution of the system. In the future work, we would consider to develop a WS-SPRM system based on total internal reflection fluorescence (TIRF) structure. Consequently, the aberration of the coupling prism can be eliminated, and the spatial resolution can be increased as well due to the objective lens with high numerical aperture and TIRF structure design. Parallelism of incident light is another factor affecting the spatial resolution of the system. The halogen lamp used in the system as the light source can avoid speckle noise caused by incoherent light source, but it is difficult to collimate. The incident light with low parallelism could cause mutual interference between different detection sites on the sensing surface, which would affect the spatial resolution. By utilizing specially-designed aspheric lens as the collimating lens group, the parallelism of incident light can be improved.

The time resolution of the system, determined by the measurement time, is 1 s for completing a wavelength-scanning and SPR imaging cycle, in which it takes about 30 ms for the LCTF to switch the wavelength of the incident light and 20 ms for the CMOS device to image the sensing surface. The time for wavelength-scanning could be shorten by replacing the LCTF with one device that offers shorter wavelength-switching time. The intensity of light source is another factor that limits the time resolution. By increasing the intensity of the light source, the exposure time of the CMOS device could be reduced.

The third aspect of improvement that needs to be considered is the sensitivity of the system. Firstly, the weak light intensity near the resonance wavelength is susceptible to external interference and dark noise of the detector, which is the main reason for limiting the sensitivity of WS-SPRM. Increasing the intensity of incident light can improve the anti-noise capacity of the system and reduce the calculating error of resonance wavelength, which is beneficial for the enhancement of system sensitivity. Secondly, in wavelength-interrogated mode, the full width at half maximum (FWHM) of incidence light that emitted from wavelength-scanning device is one of the key factors that limits the sensitivity of the system. The smaller the FWHM of incidence light is, the higher sensitivity of the system would have. Thus, the sensitivity of the system could be enhanced by replacing the LCTF with one device that offers smaller FWHM light.

4. Conclusions

This paper, for the first time, presents a WS-SPRM as a label-free and efficient analytical approach for measuring cell-substrate interactions. It allows us to monitor the changes of cell behaviors during cell detachment under the stimulation of chemicals and electroporation in a real time manner. Compared with the I-SPRM, the WS-SPRM exhibits larger dynamic range, which is beneficial for the imaging of cell adhesion. Although there are still many works to be done to improve the resolution and sensitivity of the WS-SPRM, the new reported system may be considered as a promising platform for broad applications in cell research such as cell-based clinical diagnosis, intracellular processes monitoring, cell–stimulus interactions and the binding kinetics of cell surface protein.

CRediT authorship contribution statement

Youjun Zeng: Methodology, Validation, Investigation, Writing - original draft. **Jie Zhou:** Conceptualization, Methodology, Validation, Writing - original draft, Funding acquisition, Investigation. **Xueliang Wang:** Investigation. **Zhiwen Cai:** Investigation. **Yonghong Shao:** Conceptualization, Resources, Writing - review & editing, Supervision, Funding acquisition.

Declaration of competing interest

The authors declare that they have no known competing financial interests or personal relationships that could have appeared to influence the work reported in this paper.

Acknowledgement

This work was supported by the Project from National Natural Science Foundation of China (61775148, 61527827); National Key Research and Development Program of China (2017YFB0403804); Guangdong Natural Science Foundation and Province Project (2017B020210006, 2018A030310544); Shenzhen Science and Technology R&D and Innovation Foundation (JCYJ20180305124754860).

Appendix A. Supplementary data

Supplementary data to this article can be found online at https://doi.org/10.1016/j.bios.2019.111717.

References

Abadian, P.N., Kelley, C.P., Goluch, E.D., 2014. Cellular analysis and detection using surface plasmon resonance techniques. Anal. Chem. 86 (6), 2799–2812.
Altintas, Z., Fakanya, W.M., SPR-Based Biosensor Technologies in Disease Detection and Diagnostics.
Baccar, H., Mejri, M.B., Hafaiedh, I., Ktari, T., Aouni, M., Abdelghani, A., 2010. Surface plasmon resonance immunosensor for bacteria detection. Talanta 82 (2), 810–814.
Chabot, V., Cuerrier, C.M., Escher, E., Aimez, V., Grandbois, M., Charette, P.G., 2009. Biosensing based on surface plasmon resonance and living cells. Biosens. Bioelectron. 24 (6), 1667–1673.
Chen, J.Y., Shahid, A., Garcia, M.P., Penn, L.S., Xi, J., 2012. Dissipation monitoring for assessing EGF-induced changes of cell adhesion. Biosens. Bioelectron. 38 (1), 375–381.
Chen, K., Zeng, Y., Lei, W., Gu, D., He, J., Wu, S.Y., Ho, H.P., Li, X., Qu, J., Gao, B.Z., 2016. Fast spectral surface plasmon resonance imaging sensor for real-time high-throughput detection of biomolecular interactions. J. Biomed. Opt. 21 (12), 127003.
Fen, Y.W., Yunus, W.M.M., 2013. Surface plasmon resonance spectroscopy as an alternative for sensing heavy metal ions: a review. Sens. Rev. 33 (4), 1126–1131.
Figueira, T.N., Freire, J.M., Cunhasantos, C., Heras, M., Gonçalves, J., Moscona, A., Porotto, M., Veiga, A.S., Castanho, M.A.R.B., 2017. Quantitative analysis of molecular partition towards lipid membranes using surface plasmon resonance. Sci. Rep. 7, 45647.
Hegnerová, K., Homola, J., 2010. Surface plasmon resonance sensor for detection of bisphenol A in drinking water. Sens. Actuators B Chem. 151 (1), 177–179.
Horii, M., Shinohara, H., Iribe, Y., Suzuki, M., 2011. Living cell-based allergen sensing using a high resolution two-dimensional surface plasmon resonance imager. Analyst 136 (13), 2706–2711.
J Bianca, B., Lokate, A.M.C., Besselink, G.A.J., Pruijn, G.J.M., Schasfoort, R.B.M., 2008. Angle-scanning SPR imaging for detection of biomolecular interactions on microarrays. Biosens. Bioelectron. 23 (6), 839–844.
Jennifer, A., Maynard, N.C.L., Sutherland, Jamie N., Antoine, Lesuffleur, Warrington, Arthur E., Rodriguez, Moses, Oh, Sang-Hyun, 2009. Next generation SPR technology of membrane-bound proteins for ligand screening and biomarker discovery. Biotechnol. J. 4 (11), 1542–1558.
Jie, Z., Wu, C., Tu, J., Yun, L., Ning, H., Zhang, Y., Su, K., Ping, W., 2013. Assessment of cadmium-induced hepatotoxicity and protective effects of zinc against it using an improved cell-based biosensor. Sens. Actuators A Phys. 199 (9), 156–164.
Khalili, A.A., Ahmad, M.R., 2015. A review of cell adhesion studies for biomedical and biological applications. Int. J. Mol. Sci. 16 (8), 18149–18184.
Kosaihira, A., Ona, T., 2008. Rapid and quantitative method for evaluating the personal

therapeutic potential of cancer drugs. Anal. Bioanal. Chem. 391 (5), 1889.
Laplatine, L.c., Leroy, L.c., Calemczuk, R., Baganizi, D., Marche, P.N., Roupioz, Y., Livache, T., 2014. Spatial resolution in prism-based surface plasmon resonance microscopy. Opt. Express 22 (19), 22771–22785.
Lidstone, E.A., Chaudhery, V., Kohl, A., Chan, V., Wolfjensen, T., Schook, L.B., Bashir, R., Cunningham, B.T., 2011. Label-free imaging of cell attachment with photonic crystal enhanced microscopy. Analyst 136 (18), 3608–3615.
Maltais, J.S., Denault, J.B., Gendron, L., Grandbois, M., 2012. Label-free monitoring of apoptosis by surface plasmon resonance detection of morphological changes. Apoptosis 17 (8), 916–925.
MORE, J.J., 1978. The Levenberg-Marquardt algorithm : implementation and theory in numerical analysis. Lect. Notes Math. 630, 105–116.
Olaru, A., Bala, C., Jaffrezic-Renault, N., Aboul-Enein, H.Y., 2015. Surface plasmon resonance (SPR) biosensors in pharmaceutical analysis. Crit. Rev. Anal. Chem. 45 (2), 97–105.
Peterson, A.W., Halter, M., Tona, A., Bhadriraju, K., Plant, A.L., 2009. Surface plasmon resonance imaging of cells and surface-associated fibronectin. BMC Cell Biol. 10 (1), 16.
Retra, K., Irth, H., 2011. Surface Plasmon Resonance biosensor analysis as a useful tool in FBDD. Drug Discov. Today Technol. 7 (3), e181–e187.
Reyes, P.I., Duan, Z., Lu, Y., Khavulya, D., Boustany, N., 2013. ZnO nanostructure-modified QCM for dynamic monitoring of cell adhesion and proliferation. Biosens. Bioelectron. 41 (1), 84–89.
Shinohara, H., Sakai, Y., Mir, T.A., 2013. Real-time monitoring of intracellular signal transduction in PC12 cells by two-dimensional surface plasmon resonance imager. Anal. Biochem. 441 (2), 185–189.
Stojanović, I., Schasfoort, R.B., Terstappen, L.W., 2014. Analysis of cell surface antigens by Surface Plasmon Resonance imaging. Biosens. Bioelectron. 52 (1), 36–43.
Susloparova, A., Koppenhöfer, D., Law, J.K., Vu, X.T., Ingebrandt, S., 2015. Electrical cell-substrate impedance sensing with field-effect transistors is able to unravel cellular adhesion and detachment processes on a single cell level. Lab Chip 15 (3), 668.
Tu, L., Li, X., Bian, S., Yu, Y., Li, J., Huang, L., Liu, P., Wu, Q., Wang, W., 2017. Label-free and real-time monitoring of single cell attachment on template-stripped plasmonic nano-holes. Sci. Rep. 7 (1), 11020.
Ungai-Salanki, R., Peter, B., Gerecsei, T., Orgovan, N., Horvath, R., Szabo, B., 2019. A practical review on the measurement tools for cellular adhesion force. Adv. Colloid Interface Sci. 269, 309–333.
Wang, Q., Liu, R., Yang, X., Wang, K., Zhu, J., He, L., Li, Q., 2016. Surface plasmon resonance biosensor for enzyme-free amplified microRNA detection based on gold nanoparticles and DNA supersandwich. Sens. Actuators B Chem. 223, 613–620.
Wang, W., Foley, K., Shan, X., Wang, S., Eaton, S., Nagaraj, V.J., Wiktor, P., Patel, U., Tao, N., 2011. Single cells and intracellular processes studied by a plasmonic-based electrochemical impedance microscopy. Nat. Chem. 3 (3), 249.
Wang, W., Yang, Y., Wang, S., Nagaraj, V.J., Liu, Q., Wu, J., Tao, N., 2012. Label-free measuring and mapping of binding kinetics of membrane proteins in single living cells. Nat. Chem. 4 (10), 846.
Wang, Y., Ye, Z., Si, C., Ying, Y., 2013. Monitoring of Escherichia coli O157:H7 in food samples using lectin based surface plasmon resonance biosensor. Food Chem. 136 (3-4), 1303–1308.
Wei, W., Shaopeng, W., Qiang, L., Jie, W., Nongjian, T., 2012. Mapping single-cell-substrate interactions by surface plasmon resonance microscopy. Langmuir Acs J. Surf. Colloid. 28 (37), 13373.
Yanase, Y., Hiragun, T., Ishii, K., Kawaguchi, T., Yanase, T., Kawai, M., Sakamoto, K., Hide, M., 2014. Surface plasmon resonance for cell-based clinical diagnosis. Sensors 14 (3), 4948.
Yanase, Y., Hiragun, T., Kaneko, S., Gould, H.J., Greaves, M.W., Hide, M., 2010. Detection of refractive index changes in individual living cells by means of surface plasmon resonance imaging. Biosens. Bioelectron. 26 (2), 674–681.
Yanase, Y., Hiragun, T., Yanase, T., Kawaguchi, T., Ishii, K., Hide, M., 2012. Evaluation of peripheral blood basophil activation by means of surface plasmon resonance imaging. Biosens. Bioelectron. 32 (1), 62–68.
Yanase, Y., Hiragun, T., Yanase, T., Kawaguchi, T., Ishii, K., Hide, M., 2013. Application of SPR imaging sensor for detection of individual living cell reactions and clinical diagnosis of type I allergy. Allergol. Int. 62 (2), 163–169.
Yanase, Y., Sakamoto, K., Kobayashi, K., Hide, M., 2016. Diagnosis of immediate-type allergy using surface plasmon resonance. Opt. Mater. Express 6 (4), 1339.
Zeidan, E., Kepley, C.L., Sayes, C., Sandros, M.G., 2015. Surface plasmon resonance: a label-free tool for cellular analysis. Nanomedicine 10 (11), 1833–1846.
Zeng, Y., Wang, L., Wu, S.-Y., He, J., Qu, J., Li, X., Ho, H.-P., Gu, D., Gao, B.Z., Shao, Y., 2016. High-throughput imaging surface plasmon resonance biosensing based on an adaptive spectral-dip tracking scheme. Opt. Express 24 (25), 28303–28311.
Zeng, Y.J., Hu, R., Wang, L., Gu, D.Y., He, J.N., Wu, S.Y., Ho, H.P., Li, X.J., Qu, J.L., Gao, B.Z., Shao, Y.H., 2017. Recent advances in surface plasmon resonance imaging: detection speed, sensitivity, and portability. Nanophotonics 6 (5), 1017–1030.
Ziblat, R., Lirtsman, V., Dan, D., Aroeti, B., 2006. Infrared surface plasmon resonance: a novel tool for real time sensing of variations in living cells. Biophys. J. 90 (7), 2592–2599.